Nanoscale

PAPER

CrossMark
← click for updates

Constructing bulk defective perovskite SrTiO₃ nanocubes for high performance photocatalysts†

Guoqiang Zhang,[a] Wenshuai Jiang,[b] Shixin Hua,[b] Haifeng Zhao,[a] Ligong Zhang[a] and Zaicheng Sun*[b]

Defects (Ti³⁺ or oxygen vacancies) have been demonstrated to promote the charge separation process in TiO₂ based photocatalysts. Particularly, the bulk defects within a certain concentration can give a great enhancement for both light absorption and charge separation efficiency. In this report, we explored a one-step molten salts route to synthesize SrTiO₃ nanocubes with bulk defects (Ti³⁺ doped) by using SrCO₃ as a Sr source, and TiO₂ and Ti powder as Ti sources. The amount of defects can be tuned by changing the molar ratio of Ti/TiO₂. The corresponding bandgap of SrTiO₃ can be changed from 3.29 to 2.73 eV with the increase of defects. X-ray diffraction and electron microscopy disclose that SrTiO₃ is highly crystalline and has a cubic morphology. X-ray photoelectron spectroscopy and electron paramagnetic resonance indicate that the as-prepared SrTiO₃ is close to the Ti³⁺ doped SrTiO₃. Surface photovoltage spectroscopy (SPS) and field-induced SPS confirm that Ti³⁺ doping in the SrTiO₃ turns it from an n-type semiconductor to p-type. The SrTiO₃ with an optimal amount of defects exhibits highly enhanced photocatalytic performance. An excess amount of defects results in a weak SPS response and photocatalytic performance.

Introduction

Perovskite-type materials have been extensively studied because of their wide applications as catalytic, oxygen-transport, ferroelectric, piezoelectric, and dielectric materials.[1–4] Strontium titanate (SrTiO₃) is a typical perovskite oxide that is capable of tuning chemical and physical properties by altering its composition. For example, it is easily converted into an n-type semiconductor at room temperature by either reduction or doping.[5–10] For this reason, SrTiO₃ has also been investigated as a photocatalytic[11–13] and thermoelectric material.[14,15] The pristine SrTiO₃ with a wide bandgap of 3.3 eV exhibits super photo, thermal and chemical stability. Numerous studies have been performed to improve the photocatalytic activity of SrTiO₃, such as tailoring the morphology to increase the surface area,[16–18] doping with heteroatoms to tune the bandgap,[6–8,10] and loading a cocatalyst to promote the charge separation.[19,20] In the photocatalysis process, the rapid recombination of photo-generated carriers limits the

photocatalytic efficiency of SrTiO₃. Recently, it has been demonstrated that introducing defects (such as oxygen vacancies) to a photocatalyst, for example TiO₂, can narrow the bandgap and extend the visible light absorption. More importantly, it can greatly promote the charge separation efficiency and enhance the photocatalytic performance of the photocatalyst. Our group illustrated that both surface and bulk defects have a similar function,[21] even the bulk defects work better for visible light photocatalytic activity enhancement.[21–23] Therefore, SrTiO₃ materials with a defective crystal structure and tuned bandgap are interesting and potentially beneficial to photocatalytic applications. The pristine SrTiO₃ could be treated by chemical reduction and arc-melting to obtain SrTiO₃ with surface oxygen vacancy defects.[9,24] In general, perovskite SrTiO₃ will be produced with a small surface area and free of defects because it is synthesized via a high temperature solid phase synthesis route under air. Although a few groups reported that SrTiO₃ could be synthesized via a hydrothermal route, oxygen vacancy free SrTiO₃ was obtained even in hydrazine media.[25] It is still a challenge to directly obtain defective SrTiO₃ via a chemical synthesis route and keep SrTiO₃ in nanoscale size as well.

Herein, we have developed a simple one-step molten salts route to synthesize SrTiO₃ nanocubes by employing TiO₂ as a Ti source, and SrCO₃ as a Sr source in NaCl and KCl mixed molten salts at 700 °C. To obtain defective SrTiO₃, Ti powder was chosen as a secondary Ti source, Ti was partially oxidized

ᵃState Key Laboratory of Luminescence and Applications, Changchun Institute of Optics, Fine Mechanics and Physics, Changchun, 130033 Jilin, P. R. China
ᵇBeijing Key Laboratory of Green Catalysis and Separation Department of Chemistry, Chemical Engineering School of Environmental and Energy, University of Beijing Technology, Beijing, 100022, P. R. China. E-mail: sunzc@bjut.edu.cn
†Electronic supplementary information (ESI) available: More SEM, TEM, XRD, and XPS data are shown. See DOI: 10.1039/c6nr04859e

in the reaction to form Ti^{3+} doped $SrTiO_3$, which introduces an impurity energy band below the conduction band of $SrTiO_3$. This narrows the bandgap of $SrTiO_3$ from 3.29 to 2.73 eV. The color of $SrTiO_3$ turns from light blue to dark blue with the increase of oxygen vacancies (Ti^{3+}). When the molar ratio of Ti/TiO_2 is about 5:7, the defective $SrTiO_3$ shows an optimum H_2 production rate of 311.8 μmol h^{-1} and 8.48 μmol h^{-1} for 50 mg of samples under UV-Vis light and visible light ($\lambda >$ 420 nm) irradiation, which is 2.7 times (UV-Vis) and 40.4 times ($\lambda >$ 420 nm) that of pristine $SrTiO_3$. To understand the function of the defects, surface photovoltage spectroscopy was employed to explore the effect of defects on the charge separation process. Surface photovoltage spectroscopy (SPS) illustrates that the pristine $SrTiO_3$ nanocube exhibits a typical n-type semiconductor character. Introducing Ti^{3+} into $SrTiO_3$ results in a p-type semiconductor nature. Field-induced SPS further confirms the change of conduction type. An excess amount of Ti^{3+} in $SrTiO_3$ may produce a deep energy band as a recombination center for photogenerated charges. Ti^{3+} doping may also alter the conductivity of $SrTiO_3$; these factors result in a weak or disappeared SPS response.

Experimental

Chemicals and materials

$SrCO_3$ (AR, 99.8%) and titanium (metal) crushed sponge (Ti, AR, 99.5%) are purchased from Aladdin Reagent Company. Methanol (AR, 99.5%), NaCl (AR, 99.8%) and KCl (AR, 99.8%) are purchased from Sinopharm Chemical Reagent Company. P25 TiO_2 is purchased from Degussa AG, Germany. All chemicals are used without any further purification.

Synthesis of $SrTiO_3$ (0–9 : 12–3) nanocubes

In the typical synthesis of $SrTiO_3$ nanocubes, $SrCO_3$, Ti powder, TiO_2, NaCl and KCl are mixed in an overall stoichiometric ratio of $1 : (x/12) : (1 - x/12) : 50 : 50$ ($x = 0, 3, 4, 5, 6, 7$ and 9; $Ti/TiO_2 = x/(12 - x)$). The mixtures are put into an alumina crucible and then heated to 700 °C at a rate of 5 °C min^{-1} in a muffle furnace and maintained at this temperature for 5 h. After cooling down to room temperature, the samples are washed with deionized distilled water several times to remove the remaining salt impurity and dried in an oven at 60 °C for 12 h.

Characterization

Scanning electron microscopy (SEM) images are obtained on a JEOL JSM 4800F. Transmission electron microscopy (TEM) images are obtained using an FEI Tecnai G2 operated at 200 kV. The crystalline structure is recorded by using an X-ray diffractometer (XRD) (Bruker AXS D8 Focus), using Cu Kα radiation ($\lambda = 1.54056$ Å). The Brunauer–Emmett–Teller (BET) specific surface area is measured using a Micromeritics Gemini V Surface Area and Pore Size Analyzer. X-ray photoelectron spectroscopy (XPS) analyses are performed on an ESCALABMKII spectrometer with an Al-Kα (1486.6 eV) achromatic X-ray source. The UV-Vis

absorption spectra are recorded on a UV-3600 UV-Vis-NIR scanning spectrophotometer (Shimadzu). Electron paramagnetic resonance (EPR) spectroscopy was performed on a JEOL JES-FA200 EPR spectrometer at 9.45 GHz at 300 K.

Photocatalytic activity measurements

50 mg of sample photocatalyst loaded with 1.0 wt% Pt is placed into an aqueous methanol solution (120 mL, 25 vol%) in a closed gas circulation system (Perfect Light Company Labsolar-III (AG)). UV-Vis light and visible light irradiation are obtained from a 300 W Xe lamp (PLS-SXE 300, Beijing Trusttech Co. Ltd, China) without and with a UVCUT-420 nm filter (Newport), respectively. The evolved gases are detected *in situ* by using an online gas chromatograph (GC-2014C, Shimadzu) equipped with a thermal conductivity detector (TCD).

Surface photovoltage measurements

The surface photovoltage (SPV) measurement system consists of a source of monochromatic light, a lock-in amplifier (SR 830-DSP) with a light chopper (SR 540) and a sample chamber. Monochromatic light is provided by using a 300 W Xe lamp (PLS-SXE 300, Beijing Trusttech Co. Ltd, China) and a monochromator (SBP500, Zolix). All measurements are operated at room temperature and under ambient pressure and samples are not pretreated prior to the SPV measurement.

Photoelectrode preparation

50 mg of samples is dispersed in 100 mL of 0.2 mg mL^{-1} I_2/acetone solution under ultrasonic treatment. A two electrode process is used to deposit the samples at the applied potential of 30 V for 5 min. FTO glass substrates with the coated area of about 1×3 cm^2 are used for both electrodes. Then, the deposited electrode is dried at 200 °C for 30 min to remove I_2 residues.

Photoelectrochemical measurements

A conventional three electrode process is used to investigate the photoelectrochemical properties of samples in a quartz cell. FTO photoanode deposited samples, Ag/AgCl, and Pt foil electrode act as the working electrode, reference electrode, and counter electrode, respectively. A 1.0 M NaOH aqueous solution is used as the electrolyte. The photoanode is illuminated with a 300 W Xe lamp (PLS-SXE 300, Beijing Trusttech Co. Ltd, China) with a monochromator. The illuminated area is about 1×0.5 cm^2. The IPCE (incident photon-to-current conversion efficiency) is calculated using the following equation:

$$\text{IPCE}\,(\%) = \frac{1240 \times \text{photocurrent density (mA cm}^{-2})}{\text{wavelength (nm)} \times \text{photon flux (mW cm}^{-2})} \times 100$$

Results and discussion

In general, perovskite oxides were synthesized *via* a high temperature solid phase reaction route, leading to a relatively small

surface area and low catalytic activity. In addition, the reaction was carried out in air at high temperature (~1200 °C), resulting in an oxygen vacancy free oxide. In order to obtain $SrTiO_3$ with nanostructures, we developed a molten salts route to synthesize $SrTiO_3$ nanocubes using $SrCO_3$ as a Sr source and TiO_2 as a Ti source. To introduce oxygen vacancies into the $SrTiO_3$ nanocubes, Ti powder was employed as a secondary Ti source. In the reaction, Ti was oxidized to form Ti^{3+} or oxygen vacancies in the $SrTiO_3$ nanotubes. Fig. S1† shows the optical images of $SrTiO_3$ prepared from different molar ratios of Ti/TiO_2 (m/n, where m = 0–9, n = 12–3, $m + n$ = 12, denoted as $SrTiO_3$ $m:n$). The color of the as-prepared $SrTiO_3$ samples gradually turns from white to light blue and finally into dark blue with the increasing fraction of Ti powder. The blue color indicates that the as-prepared samples may contain Ti^{3+}, in other words the as-prepared sample contains oxygen vacancies. Fig. S2† and Fig. 1A show the scanning electron microscopy (SEM) images of $SrTiO_3$ $m:n$ with cubic morphology and uniform size. Fig. 1B, S3 and S4† show the transmission electron microscopy (TEM) images, the corresponding particle size distribution and high resolution TEM images. TEM images disclose that the side length of nanocubes is about 70 nm. Each nanocube is a single crystalline particle with a clear lattice fringe spacing of 0.276 nm in the (110) direction of $SrTiO_3$. Powder X-ray diffraction (XRD) patterns of $SrTiO_3$ $m:n$ are shown in Fig. S5.† All samples exhibit a typical cubic phase with the diffraction peaks at 22.78, 32.42, 39.98, 46.49, 57.80, 67.81 and 77.18 degrees, which are related to the (100), (110), (111), (200), (211), (220) and (310) of cubic phase $SrTiO_3$ (JCPDS no. 35-0734), and no additional diffraction peaks of other species are observed. According to the Scherrer

equation, the nanocube size is calculated to be ~66 nm by using the (110) reflection peak, in agreement with the TEM results. Diffuse reflective UV-Vis spectroscopy is presented in Fig. 1C. Compared with $SrTiO_3$ 0 : 12, a stronger broad absorption band in the visible-light region is observed with the increasing molar ratio of Ti/TiO_2. These results match well with the color change of this series of samples (Fig. S1†). The Tauc plot of these $SrTiO_3$ samples is shown in Fig. 1D. The optical bandgap of $SrTiO_3$ changes from 3.29 eV for $SrTiO_3$ 0 : 12 to 3.16 eV for $SrTiO_3$ 5 : 7 and finally reaches 2.73 eV for $SrTiO_3$ 9 : 3. This indicates that the bandgap can be tuned by introducing the defects into $SrTiO_3$. According to previous reports,[9,21,26] a defect energy band is introduced below the conduction band of $SrTiO_3$, thus a narrowed bandgap is observed.

X-ray photoelectron spectroscopy (XPS, Fig. S6†) and electron paramagnetic resonance (EPR) spectroscopy are employed to further confirm the as-prepared $SrTiO_3$ with Ti^{3+} or oxygen vacancies. Fig. 2A and B show the high resolution XPS spectrum of Sr 3d and Ti 2p of $SrTiO_3$ (0 : 12, 3 : 9, 5 : 7 and 9 : 3). Both the peaks of Sr 3d and Ti 2p slightly shift to high binding energy gradually with the increasing molar ratio of Ti/TiO_2. This whole XPS peak shift is a characteristic shift of the Fermi level.[27,28] The defects like oxygen vacancies and/or Ti^{3+} increase the equilibrium electron density and push the Fermi level upwards and therefore increase the measured binding energies.[9,29] The O 1s high resolution XPS spectra (Fig. 2C) of $SrTiO_3$ (0 : 12 and 5 : 7) can be described as the superposition of three peaks by Gaussian distribution, located around 529.2 eV, 530.0 eV and 531.9 eV, respectively. The O 1s peak at 529.2 eV is usually assigned to bridging oxygen on the $SrTiO_3$ surface.[30] The peak at 530.0 eV is associated with the O^{2-} ions
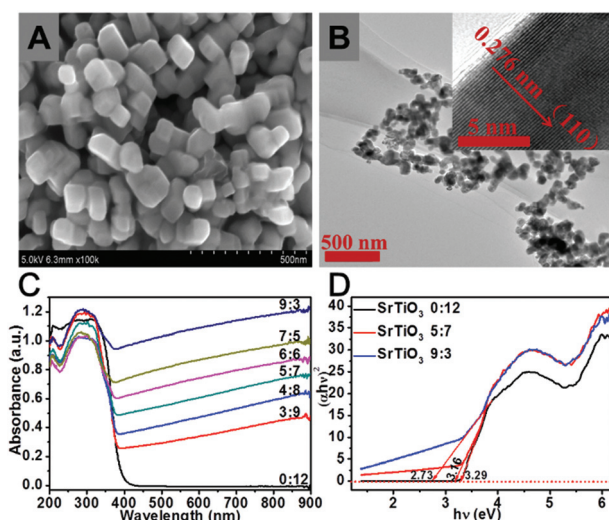
Fig. 1 Field emission scanning electron microscopy (FE-SEM) image (A), transmission electron microscopy (TEM) image (B) and high resolution TEM image (inset of B) of $SrTiO_3$ 5 : 7. Diffusion reflection UV-Vis spectra (C) of $SrTiO_3$ (0 : 12, 3 : 9, 4 : 8, 5 : 7, 6 : 6, 7 : 5 and 9 : 3). (D) is the Tauc plot of transformed Kubelka−Munk function vs. the energy of $SrTiO_3$ (0 : 12, 5 : 7 and 9 : 3).
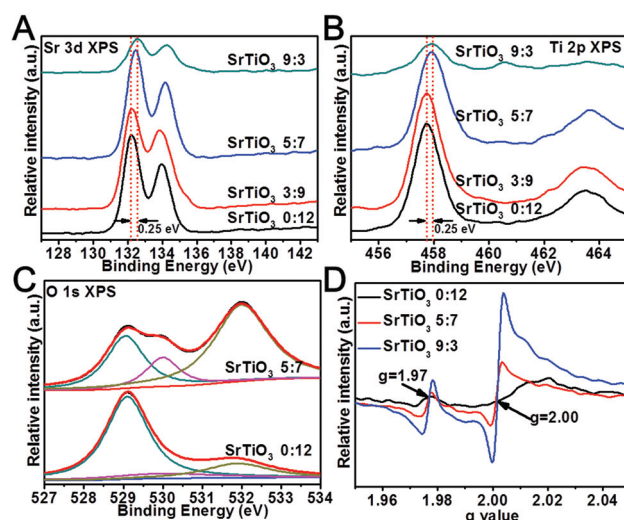
Fig. 2 X-ray photoelectron spectroscopy (XPS) of Sr 3d (A) and Ti 2p (B) of $SrTiO_3$ (0 : 12, 3 : 9, 5 : 7 and 9 : 3). The O 1s XPS spectra (C) of $SrTiO_3$ (0 : 12 and 5 : 7) can be described as the superposition of three peaks by Gaussian distribution, located around 529.2 eV, 530.0 eV and 531.9 eV, respectively. (D) is the electron paramagnet resonance (EPR) spectra of $SrTiO_3$ (0 : 12, 5 : 7 and 9 : 3).

in the crystal structure.[9,31] And the peak at 531.9 eV is attributed to O^{2-} in the oxygen defects.[9,32] In Fig. 2C, the peak at 531.9 eV presents an obvious improvement implying that the oxygen vacancy concentration increases compared with $SrTiO_3$ 0 : 12. As shown in Fig. 2D, the EPR signal observed in $SrTiO_3$ 0 : 12, 5 : 7 and 9 : 3 with $g = 1.97$ can be attributed to paramagnetic Ti^{3+},[26,33] and $g = 2.00$ is assigned to Ti^{3+} in the vicinity of oxygen vacancies in the $SrTiO_3$ lattice structure.[34–36] The signal intensity increases from $SrTiO_3$ 0 : 12 to 9 : 3, indicating that the oxygen vacancy concentration increases with the increasing molar ratio of Ti/TiO_2. The valance band (VB) XPS of $SrTiO_3$ (0 : 12, 3 : 9, 5 : 7 and 9 : 3) are shown in Fig. S7.† The VB of $SrTiO_3$ is located at ~1.71 eV below the Fermi level and no obvious shift is observed with the introduction of defects, which remains the same as previous reports.[9]

Surface photovoltage spectroscopy (SPS) is a powerful tool to characterize charge separation at the nanoscale.[37] It was recorded on powder samples sandwiched between an ITO electrode and the Cu substrate. Fig. 3A shows the surface photovoltage (SPV) response of $SrTiO_3$ nanocubes (0 : 12, 3 : 9, 5 : 7 and 9 : 3). A strong SPV response band in the range 3.3–4.0 eV is observed, which is assigned to the electron transition from the valence band to the conduction band of $SrTiO_3$ (band–band transition). According to the principle of SPS, n-type semiconductors give a positive response due to energy band bending up at the interface between the n-type semiconductor and metal. And photogenerated electrons tend to flow inside of the semiconductor.[37] When oxygen vacancies (Ti^{3+}) were introduced into $SrTiO_3$, the SPV response turns into negative, indicating that photogenerated electrons tend to flow outside (defect site). The defective $SrTiO_3$ changes from the original n-type character into the p-type nature. We can treat the defective $SrTiO_3$ as Ti^{3+} doped $SrTiO_3$, and Ti^{3+} acts as an electron acceptor, which promotes the photogenerated electrons to rapidly inject into defect sites. This process prevents the electrons and holes from recombination. However, $SrTiO_3$ 6 : 6, 7 : 5 and 9 : 3 samples exhibit no SPV response at all. There are

the following possible reasons for this. One is that the amount of photoinduced electrons accumulating instantly at the oxygen vacancy band is so much due to excess oxygen vacancies that photoelectrons can indirectly recombine with holes. Another is that an excess amount of oxygen vacancies can produce recombination centers of photoinduced electron and hole pairs.[38] In addition, doping a semiconductor with heteroatoms (impurities or dopant) can alter the electrical conductivity by many orders of magnitude.[39] For example, Nozik found that the conductivity of Cd_2SnO_4 with oxygen vacancies can rise up about 5 orders of magnitude.[40] SPS is a technique for measuring the open voltage, which build up by light irradiation. The photocharges are hardly accumulated due to the high conductivity of the semiconductor. So, the SPV response is relatively weak for the high conductivity samples. These factors are responsible for the decrease in SPS intensity. Very recently, Osterloh demonstrated that the SPS intensity tends to decrease when the photocatalyst comes in direct contact with an electron acceptor like metal nanoparticles or redox reagents.[41] In our case, the defects (oxygen vacancies or Ti^{3+}) could work as an electron acceptor. This is the reason for a decreased SPS signal or even no signal was observed when the defects were incorporated into the $SrTiO_3$ nanocrystals.

Field-induced SPS (FISPS) is a technique that combines the electric field effect principle with SPS, it was employed to further confirm the change of conduction type of $SrTiO_3$ samples.[42] In general, the effects of an external electric field on a semiconductor mainly involve two conditions. One is that the electric field may promote the separation efficiency of the photoinduced charge carriers. The other is that the electric field may alter the barrier shape of trapping, leading to the captured charge carriers in the trap easily released. For an n-type semiconductor, when a negative bias is applied, the SPV response increases in the original direction. If a positive electric field is applied, whose direction is reverse to that of the built-in field, the intensity of the SPV response is weakened and even in the reverse direction.[43] In contrast to the n-type semiconductor, the SPS response intensity of the p-type semiconductor increases as a positive field is applied and reduces as a negative electric field is applied. Fig. 3B shows the dependence of the SPS response of $SrTiO_3$ with different amounts of oxygen vacancies. The black line is the SPV response of the sample at 0 V bias. The red dashed and blue dotted lines are the SPS response measured at −0.5 and +0.5 V bias, respectively. In the case of $SrTiO_3$ 0 : 12, the original response is positive, its intensity of SPS increases when a negative bias field is applied. The SPV signal gradually reduces and turns into a reverse response (Fig. S8†). These different responses imply that $SrTiO_3$ 0 : 12 takes on the n-type character. For the $SrTiO_3$ 3 : 9 and 5 : 7 samples, they exhibit a negative response. Their SPV response increases when the negative bias field is applied, and reduces when a negative bias field is exerted. These results further confirm that $SrTiO_3$ 0 : 12 takes on the n-type nature and $SrTiO_3$ 3 : 9 and 5 : 7 show the p-type character.

Photoluminescence (PL) spectroscopy is a powerful tool for characterization of charge separation. As shown in Fig. S9,†
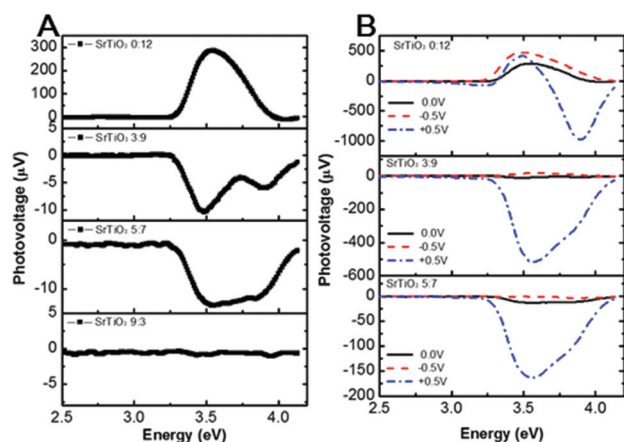

Fig. 3 Surface photovoltage spectroscopy (SPS) of $SrTiO_3$ (0 : 12, 3 : 9, 5 : 7 and 9 : 3) (A); field-induced SPS of $SrTiO_3$ (0 : 12, 3 : 9 and 5 : 7) (B).

$SrTiO_3$ exhibits emission bands at 425 and 470 nm under excitation of 380 nm light. These two emission bands reduce with the increase of defects, indicating that defects effectively suppress radiation recombination. In other words, defects promote charge separation. The Brunauer–Emmett–Teller (BET) surface area and pore size are characterized using the N_2 adsorption–desorption isotherm shown in Fig. S10.† It presents a type-III isotherm with a type-D hysteresis loop, indicating a macroporous structure.[44–46] The BET surface areas are determined to be 9.04, 11.89 and 12.41 m^2 g^{-1} of $SrTiO_3$ (0 : 12, 5 : 7 and 9 : 3), which illustrates a slight variation of the BET surface area with the increasing molar ratio (Ti/TiO_2).

Fig. 4A and S11A† show the H_2 production of $SrTiO_3$ when loaded with 1 wt% Pt as a cocatalyst under UV-Vis light (300 W Xe lamp). The H_2 production rate is 117.3 µmol h^{-1} for 50 mg of $SrTiO_3$ (0 : 12). With the increasing molar ratio (Ti/TiO_2), the H_2 production rate increases. However, an excess amount of Ti/TiO_2 (6 : 6, 7 : 5 and 9 : 3) results in a high oxygen vacancy concentration and a decrease of H_2 production rate. The optimal molar ratio (Ti/TiO_2) is about 5 : 7, and the corresponding H_2 production rate is 311.8 µmol h^{-1} (UV-Vis), which is 2.7 times that of $SrTiO_3$ (0 : 12). Although the bandgap of $SrTiO_3$ (5 : 7) is ~3.16 eV (~390 nm), the defective $SrTiO_3$ samples still exhibit a certain visible light H_2 production capability. Fig. 4B and S11B† show the H_2 production of $SrTiO_3$ under visible light irradiation ($\lambda > 420$ nm). The H_2 production rate of optimal $SrTiO_3$ 5 : 7 is 8.5 µmol h^{-1} for 50 mg of the photocatalyst. To understand this, the incident photon conversion efficiency (IPCE) is measured for $SrTiO_3$ 0 : 12 and 5 : 7 samples. Fig. 4C clearly shows that the conversion efficiency is about 5 times high at 350 nm due to the introduction of defects, indicating that defects can promote the charge separ-

ation process. The light response is up to 400 nm for $SrTiO_3$ 0 : 12. However, the light response can reach 430 nm for the $SrTiO_3$ 5 : 7 sample. These results illustrate that the defects energy band is composed of multiple energy levels. The transition between the VB and the defects energy band can also be used for H_2 production. This means the defects energy band extends the light response range. The defective $SrTiO_3$ has an excellent stability according to the recycles measure of photocatalytic H_2 production (Fig. S11C and D†). After six recycles, no reduction of photocatalytic activity is observed. These results absolutely indicate that the oxygen vacancies can narrow the bandgap of $SrTiO_3$ and promote the charge separation of photogenerated charge carriers (Fig. 4D).[47–49]

Conclusions

Defective $SrTiO_3$ nanocubes were synthesized via a one-step molten salts route by using $SrCO_3$ as a Sr source, and TiO_2 and Ti powders as a Ti source. Ti^{3+} or oxygen vacancies were successfully kept at high temperatures in air. The SPS results indicated that the conduction type turns from pristine n-type into p-type with the introduction of defects. These defects extend the $SrTiO_3$ light absorption range from the UV into the visible light region and promote the charge separation efficiency.

Acknowledgements

Notes and references

1 A. Bhalla, R. Guo and R. Roy, *Mater. Res. Innovations*, 2000, **4**, 3–26.

2 M. Pena and J. Fierro, *Chem. Rev.*, 2001, **101**, 1981–2018.

3 C. D. Chandler, C. Roger and M. J. Hampden-Smith, *Chem. Rev.*, 1993, **93**, 1205–1241.

4 M. Zeng, H. Wang, C. Zhao, J. Wei, W. Wang and X. Bai, *Sci. Bull.*, 2015, **60**, 1426–1433.

5 B. Jalan, R. Engel-Herbert, T. E. Mates and S. Stemmer, *Appl. Phys. Lett.*, 2008, 93.

6 H. Kato and A. Kudo, *J. Phys. Chem. B*, 2002, **106**, 5029–5034.

7 M. Janousch, G. I. Meijer, U. Staub, B. Delley, S. F. Karg and B. P. Andreasson, *Adv. Mater.*, 2007, **19**, 2232–2235.

8 H. Irie, Y. Maruyama and K. Hashimoto, *J. Phys. Chem. C*, 2007, **111**, 1847–1852.

9 H. Tan, Z. Zhao, W.-b. Zhu, E. N. Coker, B. Li, M. Zheng, W. Yu, H. Fan and Z. Sun, *ACS Appl. Mater. Interfaces*, 2014, **6**, 19184–19190.

10 W. L. Harrigan, S. E. Michaud, K. A. Lehuta and K. R. Kittilstved, *Chem. Mater.*, 2016, **28**, 430–433.

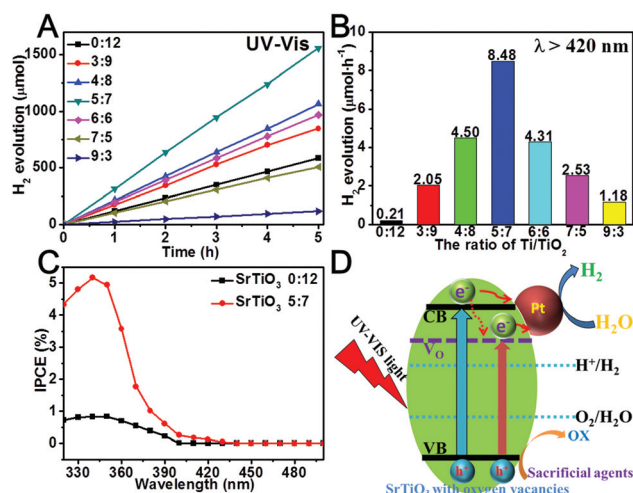11 F. Wagner and G. Somorjai, *Nature*, 1980, **285**, 559–560.

Fig. 4 (A) H_2 production of $SrTiO_3$ (0 : 12, 3 : 9, 4 : 8, 5 : 7, 6 : 6, 7 : 5 and 9 : 3) under UV-Vis light irradiation. (B) H_2 production rate of $SrTiO_3$ (0–9 : 12–3) under visible light ($\lambda > 420$ nm) irradiation. (C) IPCE of $SrTiO_3$ 0 : 12 and 5 : 7 collected at an applied potential of 0.3 V versus Ag/AgCl. The possible H_2 production mechanism (D) of defective $SrTiO_3$ under UV-Vis light irradiation.

12 S. Ouyang, H. Tong, N. Umezawa, J. Cao, P. Li, Y. Bi, Y. Zhang and J. Ye, *J. Am. Chem. Soc.*, 2012, **134**, 1974–1977.

13 L. Chen, S. Zhang, L. Wang, D. Xue and S. Yin, *J. Cryst. Growth*, 2009, **311**, 746–748.

14 S. Ohta, T. Nomura, H. Ohta, M. Hirano, H. Hosono and K. Koumoto, *Appl. Phys. Lett.*, 2005, **87**, 092108.

15 H. Ohta, S. Kim, Y. Mune, T. Mizoguchi, K. Nomura, S. Ohta, T. Nomura, Y. Nakanishi, Y. Ikuhara and M. Hirano, *Nat. Mater.*, 2007, **6**, 129–134.

16 X. Fan, Y. Wang, X. Chen, L. Gao, W. Luo, Y. Yuan, Z. Li, T. Yu, J. Zhu and Z. Zou, *Chem. Mater.*, 2010, **22**, 1276–1278.

17 J. Huang, R. Ma, Y. Ebina, K. Fukuda, K. Takada and T. Sasaki, *Chem. Mater.*, 2010, **22**, 2582–2587.

18 S. C. Yan, S. X. Ouyang, J. Gao, M. Yang, J. Y. Feng, X. X. Fan, L. J. Wan, Z. S. Li, J. H. Ye and Y. Zhou, *Angew. Chem., Int. Ed.*, 2010, **49**, 6400–6404.

19 J. Yang, D. Wang, H. Han and C. Li, *Acc. Chem. Res.*, 2013, **46**, 1900–1909.

20 L. Mei, H. Zhao and B. Lu, *Adv. Sci.*, 2015, **2**, 201500116.

21 Z. Zhao, X. Zhang, G. Zhang, Z. Liu, D. Qu, X. Miao, P. Feng and Z. Sun, *Nano Res.*, 2015, **8**, 4061–4071.

22 C. Zhou, Y. Zhao, L. Shang, Y. Cao, L.-Z. Wu, C.-H. Tung and T. Zhang, *Chem. Commun.*, 2014, **50**, 9554–9556.

23 Y. Zhao, G. Chen, T. Bian, C. Zhou, G. I. N. Waterhouse, L.-Z. Wu, C.-H. Tung, L. J. Smith, D. O'Hare and T. Zhang, *Adv. Mater.*, 2015, **27**, 7823–7823.

24 W. Yu, G. Ou, W. Si, L. Qi and H. Wu, *Chem. Commun.*, 2015, **51**, 15685–15688.

25 F. Dang, K.-i. Mimura, K. Kato, H. Imai, S. Wada, H. Haneda and M. Kuwabara, *CrystEngComm*, 2011, **13**, 3878–3883.

26 Z. Zhao, H. Tan, H. Zhao, Y. Lv, L.-J. Zhou, Y. Song and Z. Sun, *Chem. Commun.*, 2014, **50**, 2755–2757.

27 C. Lee, J. Destry and J. L. Brebner, *Phys. Rev. B: Solid State*, 1975, **11**, 2299–2310.

28 W. S. Baer, *Phys. Rev.*, 1966, **144**, 734–738.

29 T. Sun and M. Lu, *Appl. Phys. A*, 2012, **108**, 171–175.

30 T. Kawabe, K. Tabata, E. Suzuki, Y. Yamaguchi and Y. Nagasawa, *J. Phys. Chem. B*, 2001, **105**, 4239–4244.

31 S.-M. Park, T. Ikegami and K. Ebihara, *Thin Solid Films*, 2006, **513**, 90–94.

32 M. Chen, X. Wang, Y. Yu, Z. Pei, X. Bai, C. Sun, R. Huang and L. Wen, *Appl. Surf. Sci.*, 2000, **158**, 134–140.

33 F. Zuo, K. Bozhilov, R. J. Dillon, L. Wang, P. Smith, X. Zhao, C. Bardeen and P. Feng, *Angew. Chem.*, 2012, **124**, 6327–6330.

34 M. K. Kumar, K. Bhavani, B. Srinivas, S. N. Kumar, M. Sudhakar, G. Naresh and A. Venugopal, *Appl. Catal., A*, 2016, **515**, 91–100.

35 S. Livraghi, A. Votta, M. C. Paganini and E. Giamello, *Chem. Commun.*, 2005, 498–500.

36 G. Barolo, S. Livraghi, M. Chiesa, M. C. Paganini and E. Giamello, *J. Phys. Chem. C*, 2012, **116**, 20887–20894.

37 L. Kronik and Y. Shapira, *Surf. Sci. Rep.*, 1999, **37**, 1–206.

38 J. Liqiang, F. Honggang, W. Baiqi, W. Dejun, X. Baifu, L. Shudan and S. Jiazhong, *Appl. Catal., B*, 2006, **62**, 282–291.

39 H. J. Queisser and E. E. Haller, *Science*, 1998, **281**, 945–950.

40 A. J. Nozik, *Phys. Rev. B: Solid State*, 1972, **6**, 453.

41 J. Wang, J. Zhao and F. E. Osterloh, *Energy Environ. Sci.*, 2015, **8**, 2970–2976.

42 J. Liqiang, Q. Yichun, W. Baiqi, L. Shudan, J. Baojiang, Y. Libin, F. Wei, F. Honggang and S. Jiazhong, *Sol. Energy Mater. Sol. Cells*, 2006, **90**, 1773–1787.

43 X. Tengfeng, W. Dejun, Z. Lianjie, W. Ce, L. Tiejin, Z. Xueqin and W. Mang, *J. Phys. Chem. B*, 2000, **104**, 8177–8181.

44 D. Liu, Y. Yao, D. Tang, S. Tang, Y. Che and W. Huang, *Int. J. Coal Geol.*, 2009, **79**, 97–112.

45 M. Khalfaoui, S. Knani, M. Hachicha and A. B. Lamine, *J. Colloid Interface Sci.*, 2003, **263**, 350–356.

46 J. Wang, X. Yang, D. Wu, R. Fu, M. S. Dresselhaus and G. Dresselhaus, *J. Power Sources*, 2008, **185**, 589–594.

47 Z. Zhang, W. Wang, E. Gao, M. Shang and J. Xu, *J. Hazard. Mater.*, 2011, **196**, 255–262.

48 T.-T. Chen, I.-C. Chang, M.-H. Yang, H.-T. Chiu and C.-Y. Lee, *Appl. Catal., B*, 2013, **142**, 442–449.

49 L. Liu, F. Gao, H. Zhao and Y. Li, *Appl. Catal., B*, 2013, **134**, 349–358.